Automotive Innovation (2024) 7:507–528
https://doi.org/10.1007/s42154-023-00262-z

A Comprehensive Analysis on Electronic Moment Power Steering Control Strategy for Multi-axle Distributed Drive Vehicles

Hang Li[1] · Zunyan Hu[1] · Jianqiu Li[1] · Jiayi Hu[1] · Liangfei Xu[1] · Minggao Ouyang[1]

Received: 16 January 2023 / Accepted: 31 August 2023 / Published online: 11 July 2024

Abstract

The electric wheel has an advantage of independently, accurately, and promptly controlling torque in response. However, current distributed drive steering control strategies fail to fully leverage this capability. To fill this gap, this paper proposes a composite electronic moment power steering (EMPS) control strategy for multi-axle distributed drive vehicles, based on dynamic modeling and analysis. The proposed control strategy integrates EMPS with direct yaw moment control (DYC), enhancing steering flexibility and fault tolerance in the steering system at low speeds, while also ensuring vehicle stability at high velocities. It adopts a hierarchical control architecture, wherein the upper controller utilizes a nonlinear state observer for the joint estimation of multi-objective parameters, and the lower controller is responsible for the accurate tracking of the steering angle by EMPS, the yaw rate tracking by DYC, and the assignment of weights to the composite controller. By establishing and analyzing a detailed vehicle model and an electric drive steering axle dynamics model, a multi-dimensional feasible domain for EMPS is proposed, ensuring the safety and smoothness of steering maneuvers. The co-simulation of MATLAB/Simulink and TruckSim are conducted to verify the effectiveness of the composite control strategy. The EMPS controller is proved to have robust steering angle tracking performance, with the $\beta - \dot{\beta}$ trajectory consistently converging within the stability zone, maintaining a sufficient margin for tire longitudinal force under the composite steering control. Additionally, real vehicle testing confirms the effectiveness of EMPS and the redundancy tolerance of the steering functionality in distributed drive multi-axle vehicles equipped with EMPS.

Keywords Distributed drive vehicle · Electric wheel · Vehicle dynamics control · Nonlinear observer · Electronic moment power steering

Abbreviations

CG	Vehicle center of gravity
DOF	Degree of freedom
DYC	Direct raw moment control
EHPS	Electronic hydraulic power steering
EKF	Extended Kalman filter
EMPS	Electronic moment power steering
EPS	Electric Power steering
HPS	Hydralic Power steering
MS	Manual steering
PF	Particle filter
SBW	Steering by wire
SMC	Sliding mode control

1 Introduction

Multi-axle vehicles, characterized by their elongated bodies and increased mass, often exhibit reduced agility at low speeds and compromised handling stability at high speeds [1, 2]. The effectiveness of the steering control strategy in multi-axle vehicles plays a critical role in determining their flexibility, stability, reliability, safety, and efficiency. One innovative approach involves the utilization of a distributed drive system equipped with electric wheels. This configuration offers a distinct advantage, allowing for independent, precise, and rapid control of the torque applied to each wheel. Such a setup can significantly enhance the steering control performance [3–6]. This paper aims to investigate the implementation of an electric wheel-based steering control strategy for multi-axle vehicles with distributed drive systems.

Electric wheel torque allocation optimizes the steering dynamics of distributed drive vehicles in terms of improving

---

✉ Zunyan Hu
hzy6608128@163.com

[1] State Key Laboratory of Automotive Safety and Energy, Tsinghua University, Beijing, China

vehicle stability and steering characteristics. Vehicle stability control methods mainly focus on changing the yaw torque of the vehicle by varying the longitudinal forces of the left and right tires. Among these methods, direct yaw moment control (DYC) stands out as a widely adopted approach that targets the vehicle's sideslip angle and yaw rate. Various tracking controllers, such as PID controller [7, 8], fuzzy logic controller [8], sliding mode controller [9, 10], BP-PID controller [11], and robust H∞ controller [12], are commonly employed in DYC systems.

The unique ability to independently control the torque of each electric wheel in multi-axle distributed drive vehicles enables DYC to be achieved by modulating the torque differential between the left and right electric wheels, eliminating the need for traditional mechanical braking systems. Despite extensive research on vehicle stability control, the exploration of distributed electric drive systems with electric wheels in steering control for multi-axle vehicles remains relatively limited. Wang and his team [13, 14] proposed the differential drive assist steering (DDAS) control method for distributed drive vehicles with electric wheel drive systems. This technique utilizes the torque variances between the left and right front wheels to facilitate assisted steering.

However, DDAS systems for multi-axle distributed drive vehicles act on the left and right wheels of the front axle to reduce steering resistance torque during steering and enhance the steering sensation. This process operates as an open-loop control system. To enhance the steering agility of multi-axle vehicles and align with the requirements of vehicle automation and intelligence, it becomes imperative to incorporate closed-loop control mechanisms for steering angles across all steering axles. Since this control objective is similar to EHPS, and the control object is the left and right side electric wheels of each electric drive axle that generate steering moments, this study introduces the concept of electronic moment power steering (EMPS). The primary focus lies in constructing a precise nonlinear model of the vehicle and steering axle. Building upon this foundation, an EMPS control strategy is formulated, followed by a systematic analysis of the multi-dimensional feasible domain of EMPS. Subsequently, a comprehensive steering control strategy is devised, blending the EMPS and DYC methodologies for distributed drive systems. This integrated approach considers both steering flexibility and vehicle stability to optimize overall performance.

The rest of the paper is organized as follows: Sect. 2 will elaborate on the dynamics model of the multi-axle vehicle and electric drive steering axle. Section 3 will present the composite electronic moment power steering control strategy. In Sect. 4, the simulation segment will delve into a detailed discussion and comparison of simulation results obtained from the two steering controllers under various co-simulation conditions using MATLAB/Simulink and TruckSim software. A vehicle test will be conducted in Sect. 4 to validate the efficacy of the EMPS steering control strategy. Lastly, Sect. 5 will encapsulate the findings and draw conclusions based on the study's outcomes.

2 Multi-axle Vehicle Modeling and Electric Drive Axle Steering System Dynamics Analysis

Vehicle model and electric drive axle steering model for n-axle distributed electric wheel drive vehicles are built and analyzed, in order to design the composite EMPS control strategy.

2.1 Vehicle Model

2.1.1 Vehicle Coordinate System

The vehicle coordinate system (*XYZ*) is established for the planar dynamics control of distributed drive multi-axle steering vehicles, according to ISO8855/DIN70000, as shown in Fig. 1.

The longitudinal velocity of the vehicle is defined as u, the lateral velocity is defined as v, and the yaw rate is defined as γ. As shown in Fig. 2, the positive directions of the three velocities are the positive directions of X, Y, and Z axes, respectively. The vector of motion states of CG is defined as:

$$\boldsymbol{V} = (u, v, \gamma)^{\mathrm{T}} \tag{1}$$

The tire coordinate system, denoted as $x_{wij}y_{wij}z_{wij}$, where i represents the ith axle counting from the front of the vehicle and j takes values 0 and 1 for the left and right wheels, respectively, is illustrated in Fig. 2. F_{xij} and F_{yij} are defined as the longitudinal and lateral forces acting on this wheel, respectively, with the positive directions of x_{wij} and y_{wij} axes aligned in the positive direction. The force vector within the

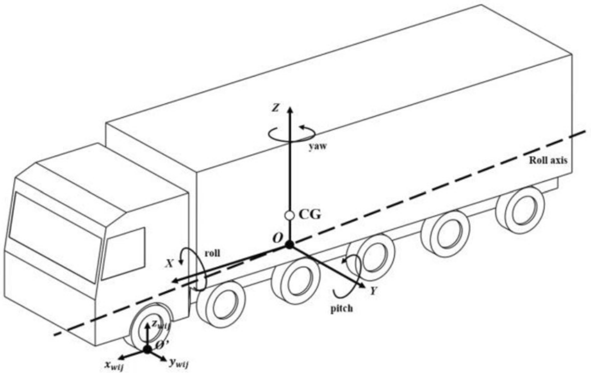

Fig. 1 Vehicle coordinate system

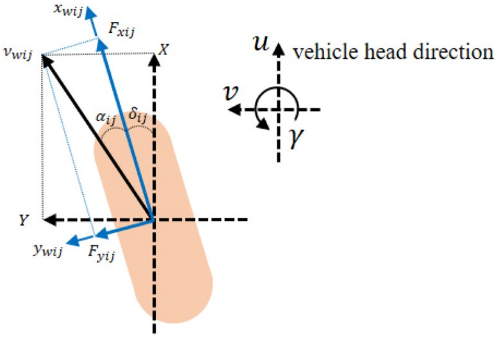

Fig. 2 Definition of vehicle coordinate system

coordinate system of each electric wheel tire is defined as follows:

$$\boldsymbol{F}_{ij} = \left(F_{xij}, F_{yij}\right)^{\mathrm{T}} \tag{2}$$

The origin of the tire coordinate system $x_{wij}y_{wij}$ is located at the center of each tire, and its position under the vehicle coordinate system XYZ is:

$$\boldsymbol{r}_{ij} = \left(x_i, b_j\right)^{\mathrm{T}} \tag{3}$$

where $i \in \{1 \sim n\}$; $b_j = (-1)^j \frac{b_w}{2}$, b_w is the vehicle track.

According to the definition, when the ith axle is located in front of CG, $x_i > 0$, otherwise, $x_i < 0$. The velocity state of each wheel center in the vehicle coordinate system is expressed as:

$$\boldsymbol{v}_{wij,V} = \boldsymbol{T}_{ij}\boldsymbol{V} \tag{4}$$

$$\boldsymbol{T}_{ij} = \begin{pmatrix} 1 & 0 & -b_j \\ 0 & 1 & x_i \end{pmatrix} \tag{5}$$

Concerning the steering relationship among the axles and ignoring the difference between the left and right wheel steering angles δ_{ij}, the steering angle of the ith axle is expressed as δ_i. Projecting $\boldsymbol{F}_{ij}$ onto the vehicle coordinate system, the resulting tire force vector is:

$$\boldsymbol{F}_{ij,V} = \boldsymbol{T}\left(\delta_i\right)\boldsymbol{F}_{ij} \tag{6}$$

where the tire force transformation matrix $\boldsymbol{T}\left(\delta_i\right)$ is related to this wheel rotation angle:

$$\boldsymbol{T}\left(\delta_i\right) = \begin{pmatrix} \cos\delta_i & -\sin\delta_i \\ \sin\delta_i & \cos\delta_i \end{pmatrix} \tag{7}$$

In the tire coordinate system, the definition and the conversion relationship of wheel center velocity are as follows:

$$\boldsymbol{v}_{wij} = \left(v_{xij}, v_{yij}\right) \tag{8}$$

$$\boldsymbol{v}_{wij} = \boldsymbol{T}^{\mathrm{T}}\left(\delta_i\right)\boldsymbol{v}_{wij,V} \tag{9}$$

2.1.2 Vehicle Dynamics Model

To describe the longitudinal-lateral coupling motion of the vehicle in detail, a vehicle planar three-degree-of-freedom (3-DOF) model is established, considering the three degrees of freedom of the motion state vector $\boldsymbol{V}$.

The combined forces on CG include the longitudinal and lateral combined forces and the yaw moment, expressed as:

$$\boldsymbol{F}_c = \left(F_x, F_y, M_z\right)^{\mathrm{T}} \tag{10}$$

According to the vehicle driving resistance equation, the wind resistance, roll resistance, and slope resistance of CG are expressed in the vehicle coordinate system as:

$$F_{df} = \frac{1}{2}\rho C_d A u^2 + mgf\cos\theta + mg\sin\theta \tag{11}$$

where ρ is air density, C_d is the vehicle wind resistance coefficient, A is the windward area, f is the roll resistance coefficient, θ is the road slope, and g is gravitational acceleration. m is the overall vehicle mass, including the unsprung mass m_{bi} and the sprung mass m_a.

$$m = m_a + \sum_{i=1}^{n} m_{bi} \tag{12}$$

The combined force on CG is calculated as:

$$\boldsymbol{F}_c = \sum_{i=1}^{n}\sum_{j=0}^{1}\begin{pmatrix} \boldsymbol{F}_{ij,V} \\ \boldsymbol{T}_{fc}^{\mathrm{T}}\boldsymbol{F}_{ij,V} \end{pmatrix} + \begin{pmatrix} F_{df} \\ 0 \\ 0 \end{pmatrix} \tag{13}$$

$$\boldsymbol{T}_{fc} = \left(-b_j, x_i\right)^{\mathrm{T}} \tag{14}$$

According to the kinematic relationship of the vehicle, the momentum theorem and momentum moment theorem, the acceleration a_x, a_y and the yaw angular acceleration $\dot{\gamma}$ of CG can be obtained by the combined force, and the dynamics equations of the planar motion of vehicle is established as follows:

$$\dot{\boldsymbol{V}} = \left(a_x, a_y, \dot{\gamma}\right)^{\mathrm{T}} = \mathbf{C}\boldsymbol{F}_c + \mathbf{T}_u(\boldsymbol{V})\boldsymbol{V} \tag{15}$$

$$\mathbf{T}_u(\boldsymbol{V}) = \begin{vmatrix} 0 & -\gamma & 0 \\ \gamma & 0 & 0 \\ 0 & 0 & 0 \end{vmatrix} \tag{16}$$

$$\boldsymbol{C} = \mathrm{diag}(m^{-1}, m^{-1}, I_z^{-1}) \tag{17}$$

where I_z is the vehicle yaw inertia.

2.1.3 Linear 2-DOF Model of a Multi-axle Vehicle

In order to study the steering motion process of multi-axle vehicles, a linear 2-DOF model of multi-axle vehicles is established with reference to the linear 2-DOF model of four-wheel vehicles [15].

Based on the small angle assumption of the linear 2-DOF model and the linear assumption of the lateral deflection characteristics of the tire, the lateral combined force of all ith axle tires is expressed as:

$$F_{Yi} = 2C_{yi}\beta_{ti} = C_i\left(\delta_i - \frac{v + \gamma x_i}{u}\right) \tag{18}$$

where C_{yi}, β_{ti} are the lateral deflection stiffness and sideslip angle of the ith axle tires, and $C_i = 2C_{yi}$.

The sideslip angle β of vehicle is calculated as follows, where the vehicle speed u is considered as a constant value in the linear 2-DOF model.

$$\beta \approx \tan\beta = \frac{v}{u} \tag{19}$$

Based on the above assumptions, the linear 2-DOF differential equations of motion of the vehicle are derived based on the dynamic equations of the planar motion of the vehicle in Eq. (15) as follows:

$$\begin{bmatrix} \dot{\beta} \\ \dot{\gamma} \end{bmatrix} = -\begin{bmatrix} \frac{\sum_i C_i}{mu} & \frac{\sum_i x_i C_i}{mu^2} + 1 \\ \frac{\sum_i x_i C_i}{I_z} & \frac{\sum_i x_i^2 C_i}{I_z u} \end{bmatrix} \begin{bmatrix} \beta \\ \gamma \end{bmatrix} + \begin{bmatrix} \frac{C_1}{mu} & \cdots & \frac{C_n}{mu} \\ \frac{x_1 C_1}{I_z} & \cdots & \frac{x_n C_n}{I_z} \end{bmatrix} \begin{vmatrix} \delta_1 \\ \cdots \\ \delta_n \end{vmatrix} + \begin{bmatrix} 0 \\ \frac{1}{I_z} \end{bmatrix} M_Z \tag{20}$$

Applying the Laplace transform to Eq. (20), the following equation can be derived:

$$\begin{bmatrix} \beta_{ss} \\ \gamma_{ss} \end{bmatrix} = \frac{\begin{bmatrix} mu\sum_i x_i^2 C_i & -I_z\left(\sum_i x_i C_i + mu^2\right) \\ -mu^2 \sum_i x_i C_i & I_z u \sum_i C_i \end{bmatrix} \begin{bmatrix} \frac{C_1}{mu} & \cdots & \frac{C_n}{mu} \\ \frac{x_1 C_1}{I_z} & \cdots & \frac{x_n C_n}{I_z} \end{bmatrix} \begin{bmatrix} \delta_1 \\ \cdots \\ \delta_n \end{bmatrix}}{\left(\sum_i C_i\right)\left(\sum_i x_i^2 C_i\right) - \left(\sum_i x_i C_i\right)^2 - mu^2 \sum_i x_i C_i} \tag{21}$$

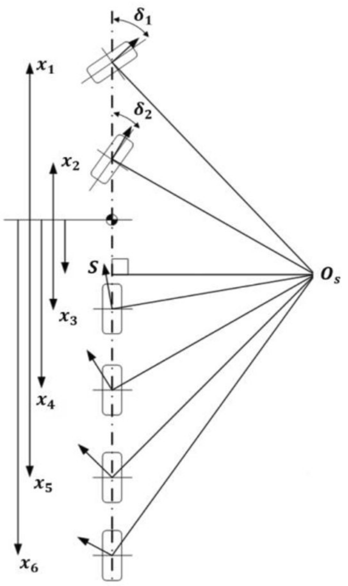

Fig. 3 Single-track model of multi-axle vehicle

Taking the steering angle and the tire sideslip angle of each axle tire into consideration, there exists a transient steering center O_s during the vehicle steering process, as shown in the single-track model of multi-axle vehicle in Fig. 3. To mitigate tire wear during steering maneuvers, an analysis of the full-axle steering scenario for each axle, adhering to Ackermann's steering equation, is conducted in this section. A vertical line perpendicular to the longitudinal direction of the vehicle intersects the transient steering center O_s. The coordinate of the vertical foot S point on the X-axis of the vehicle coordinate system is defined as the steering center distance x_{cs}, which is often negative. Therefore, under the small angle assumption of the linear 2-DOF model within the single-track model, the relationship between the steering angles of the axles can be described as follows:

$$\frac{\delta_i}{\delta_1} \approx \frac{\tan\delta_i}{\tan\delta_1} = \frac{x_i - x_{cs}}{x_1 - x_{cs}} \tag{22}$$

The relationship between the rear axle steering angles and the first axle steering angle is expressed as:

$$\delta_i = h_i \delta_1 \tag{23}$$

$$h_i = \frac{x_i - x_{cs}}{x_1 - x_{cs}} \tag{24}$$

Based on the axle steering angle relationship defined by Eqs. (23) and (24), the lateral motion of the vehicle is transformed from a multiple-input single-output system to a single-input single-output system. Consequently, the steady-state response of the vehicle, described in Eq. (21), can be summarized in the same form as that of a linear 2-DOF model of a conventional two-axle vehicle.

$$\beta = \frac{\left(\sum_i x_i h_i C_i\right)\left(\sum_i x_i C_i\right) - \left(\sum_i h_i C_i\right)\left(\sum_i x_i^2 C_i\right) + \left(\sum_i x_i h_i C_i\right)mu^2}{L_{\mathrm{num}} + \left(\sum_i x_i C_i\right)mu^2}\delta_1 \tag{25}$$

$$\gamma = \frac{u}{L_{\mathrm{eff}}\left(1 + K_{\mathrm{eff}}u^2\right)}\delta_1 \tag{26}$$

where

$$L_{\mathrm{eff}} = L_{\mathrm{num}} / L_{\mathrm{den}} \tag{27}$$

$$L_{\mathrm{num}} = \left(\sum_i x_i C_i\right)^2 - \left(\sum_i C_i\right)\left(\sum_i x_i^2 C_i\right) \tag{28}$$

$$L_{\mathrm{den}} = \left(\sum_i x_i C_i\right)\left(\sum_i h_i C_i\right) - \left(\sum_i C_i\right)\left(\sum_i x_i h_i C_i\right) \tag{29}$$

$$K_{\mathrm{eff}} = \left(\sum_i x_i C_i\right) m / L_{\mathrm{num}} \tag{30}$$

2.2 Electric Wheel Dynamics Model

The force analysis of the rotational dynamics model of electric wheel is shown in Fig. 4, according to which the differential equation of rotational motion of the electric wheel is established as follows:

$$I_{\mathrm{w}} \dot{\omega}_{ij} = T_{mij} - F_{xij} R \tag{31}$$

where I_{w} is the rotational inertia of the electric wheel, R is the effective radius of the electric wheel tire, T_{mij} is the output torque of each electric wheel, and ω_{ij} is the rotational speed of each electric wheel.

Calculating load transfer by acceleration is currently the most convenient and commonly used method for tire vertical force calculation [16]. Taking into account the load transfer due to the pitching and the rolling motion, the vertical load of each electric wheel is calculated as follows:

$$\begin{aligned} F_{zij} = {} & \frac{mg}{2} \frac{\left(\sum_{k=1}^{n} L_k - nL_i\right) L_{\mathrm{cg}} + \left(L_i \sum_{k=1}^{n} L_k - \sum_{k=1}^{n} L_k^2\right)}{\left(\sum_{k=1}^{n} L_k\right)^2 - n \sum_{k=1}^{n} L_k^2} \\ & + \frac{ma_x}{2} \frac{\left(\sum_{k=1}^{n} L_k - nL_i\right) h_{\mathrm{cg}}}{\left(\sum_{k=1}^{n} L_k\right)^2 - n \sum_{k=1}^{n} L_k^2} + (-1)^j \kappa_i m a_y \frac{h_{\mathrm{cg}}}{b_w} \end{aligned} \tag{32}$$

where κ_i represents the roll stiffness factor of the suspension on the ith axle, and subject to $\sum \kappa_i = 1$; h_{cg} is the height of CG; L_i and L_{cg} is the distance from the first axle to the ith axle and to CG, respectively, as shown in Fig. 5.

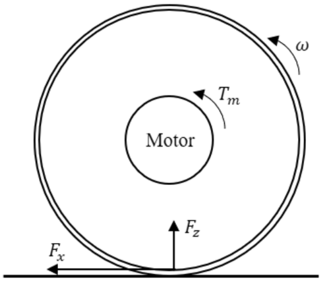

Fig. 4 Rotational dynamics model of electric wheel

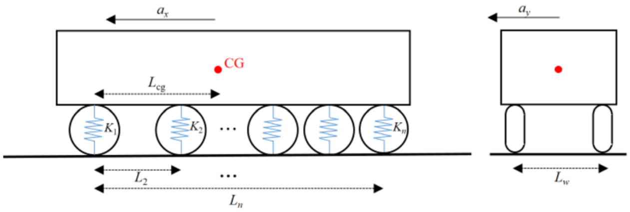

Fig. 5 Force analysis of the vertical force of electric wheel

$$L_i = x_1 - x_i \tag{33}$$

$$L_{\mathrm{cg}} = x_1 - x_{\mathrm{cg}} \tag{34}$$

2.3 Nonlinear Tire Model

In order to calculate the longitudinal force, lateral force, and aligning torque of the tire, a tire model is required. Due to the strong nonlinearity of the tire, simple physical models can not quantitatively describe the tire's sextant force behavior, so empirical models such as the Unitire model and the H.B. Pacejke tire magic model based on experiments becomes a natural choice [17].

In this paper, the tire magic model is chosen. The advantage of the magic formula of this model is that the longitudinal force, lateral force, and aligning torque of the tire can be expressed by a set of trigonometric equations of the same form, which can provide accurate information when applied to observe vehicle condition parameters.

$$F_{xij\_\mathrm{MF}} = D_x \sin\left\{C_x \arctan\left[B_x s_{xij} - E_x\left(B_x s_{xij} - \arctan B_x s_{xij}\right)\right]\right\} \tag{35}$$

$$F_{yij\_\mathrm{MF}} = D_y \sin\left\{C_y \arctan\left[B_y \alpha_{ij} - E_y\left(B_y \alpha_{ij} - \arctan B_y \alpha_{ij}\right)\right]\right\} \tag{36}$$

$$M_{tij\_\mathrm{MF}} = D_t \sin\left\{C_t \arctan\left[B_t \alpha_{ij} - E_t\left(B_t \alpha_{ij} - \arctan B_t \alpha_{ij}\right)\right]\right\} \tag{37}$$

where B_x, B_y, and B_t are the stiffness factors; C_x, C_y, and C_t are the shape factors; D_x, D_y, and D_t are the peak factors; and E_x, E_y, and E_t are the curvature factors. These experimental parameters are related to the vertical load of the wheel and vehicle parameters such as wheel camber. s_{xij} and α_{ij} are the longitudinal slip rate of and the sideslip angle of the tire, respectively, expressed as follows:

$$s_{xij} = \frac{\omega_{ij} R - v_{xij}}{\max\left(\omega_{ij} R, v_{xij}\right)} \tag{38}$$

$$\alpha_{ij} = \arctan\left(\frac{v_{yij}}{v_{xij}}\right) = \delta_i - \arctan\left(\frac{v + \gamma x_i}{u - \gamma b_j}\right) \tag{39}$$

2.4 Electric Drive Steering Axle Dynamics Model

2.4.1 Steering Dynamics Model of Single Electric Wheel

The steering dynamics model of single electric wheel around the kingpin is depicted in Fig. 6 [18].

Based on the force analysis of this model, the differential equation of the steering dynamics of the electric wheel is written as follows:

$$M_{sij} - M_{aij} - M_{fij} = I_{sw}\ddot{\delta}_i \tag{40}$$

where I_{sw} is the wheel inertia around the kingpin, M_{sij} is the steering moment of the external steering system acting on the kingpin of the electric wheel, and M_{fij} represents the steering friction moment. M_{aij} is the aligning moment and contains the following components:

$$M_{aij} = M_{aijx} + M_{aijy} + M_{aijz} + M_{aijt} \tag{41}$$

M_{aijx}, M_{aijy}, and M_{aijz} are the aligning moment along the kingpin generated by the electric wheel drive force, the tire lateral force and the load on electric wheel, respectively.

$$M_{aijx} = F_{xij}R_x\cos\tau\cos\sigma + T_{mij}\sin\sigma \tag{42}$$

$$M_{aijy} = F_{yij}R_y\cos\tau\cos\sigma \tag{43}$$

$$M_{aijz} = F_{zij}\left(R_x + R\tan\sigma\right)\cos\tau\sin\sigma\cos\sigma\sin\delta_i \tag{44}$$

where R_x is the distance from the intersection point of the extension line of the kingpin axis and the ground to the intersection of the wheel center plane and the ground, τ the caster angle of the kingpin, σ the lateral inclination of the kingpin, R_y is the pneumatic trail, which can be expressed as:

$$R_y = R\tan\tau \tag{45}$$

M_{aijt} is the component of the tire's aligning torque around the kingpin direction:

$$M_{aijt} = M_{tij}\cos\tau\cos\sigma \tag{46}$$

2.4.2 Steering Dynamics Model of Electric Drive Steering Axle

Based on the aforementioned assumptions, the left and right wheels of electric drive steering axle have the same steering angle, and the effect of vehicle rolling motion on the steering system is ignored. Then, the aligning moment acting around the kingpin, induced by the load on both the left and right sides, is of equal magnitude but opposite direction. Additionally, the steering moment input originating from the external steering system is omitted in the differential moment steering procedure. The steering dynamics model of electric drive steering axle is shown in Fig. 7, and its differential equation of the steering dynamics is as follows:

$$M_i - M_{ayi} - M_{ati} - K_p\delta_i - C_p\dot{\delta}_i - M_{fi} = I_{si}\ddot{\delta}_i \tag{47}$$

where K_p and C_p represent the total equivalent steering stiffness and damping around the kingpin, respectively. I_{si} signifies the total rotational inertia of the left and right wheels around the kingpin. M_{fi} pertains to the total steering friction moment. M_i denotes the steering moment generated by the difference between the output torque of the left and right side electric wheels, which is also the main control object of the EMPS control strategy.

$$\Delta T_{mi} = T_{mi1} - T_{mi0} \tag{48}$$

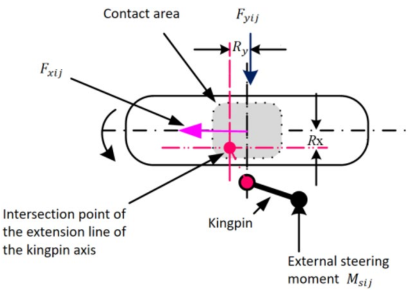

Fig. 6 Steering dynamics model of single electric wheel

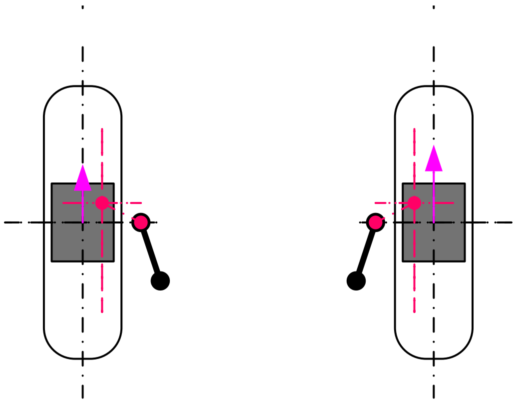

Fig. 7 Steering dynamics model of electric drive steering axle

$$M_i = \left(T_{mi1} - T_{mi0}\right)\left(\frac{R_x}{R}\cos\tau\cos\sigma + \sin\sigma\right) = \left(\frac{R_x}{R}\cos\tau\cos\sigma + \sin\sigma\right)\Delta T_{mi} \tag{49}$$

M_{ayi} and M_{ati} are the total aligning moment generated by the lateral forces and tire aligning torque, respectively.

$$M_{ayi} = \sum_{j=1,2} F_{yij} R\sin\tau\cos\sigma \tag{50}$$

$$M_{ati} = \sum_{j=1,2} M_{tij}\cos\tau\cos\sigma \tag{51}$$

To facilitate the calculation, when the tire is in the stable zone, the tire aligning torque can be approximated using the tire lateral force as follows [19]:

$$M_{tij} = F_{yij} l^2/3 \tag{52}$$

where l is half of tread contact width.

3 Composite Electronic Moment Power Steering Control Strategy

3.1 Hierarchical Coordinated Control Architecture

A hierarchical coordinated control architecture has been devised for steering control in multi-axle distributed drive vehicles. The block diagram illustrating this hierarchical control strategy is depicted in Fig. 8.

The upper controller includes a nonlinear state observer and a transient steering center distance x_{cs} calculation module. The state observer collects the vehicle state parameters required by the control system, including the longitudinal velocity u, the lateral velocity v, the yaw rate γ, and lateral force of each electric wheel F_{yij}.

The lower controller includes the EMPS controller, the DYC controller, a composite steering controller weight assignment module, and a torque constraint module. During normal steering, or in the event of a mechanical steering system failure, the EMPS controller provides the electric wheel differential torque required for axle target steering angle tracking, improving steering flexibility and providing fault-tolerant steering capability. The DYC controller provides the target yaw moment to stabilize the vehicle during high speed, steep steering. The switching judgment between the two steering controllers and the smooth transition are performed by the composite steering controller weight assignment module. Finally, the torque constraint module ensures that each electric wheel operate under stable conditions.

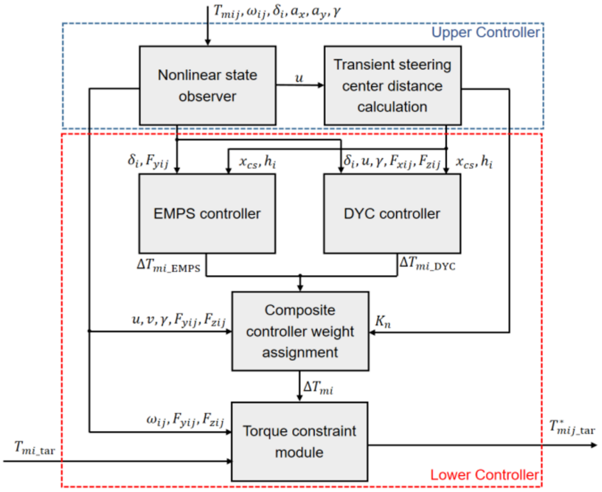

Fig. 8 Block diagram of the composite hierarchical steering control strategy

3.2 Upper Controller

3.2.1 Nonlinear State Observer

The particle filter (PF) presents an advantageous alternative to the Kalman filter by alleviating the stringent prerequisites of linearity and Gaussian error distribution within the system. It is particularly well-suited for estimating state parameters in highly nonlinear systems like vehicles. While the standard PF leverages the system state's transition probability as the importance density function, it overlooks real-time observation data. Consequently, the resulting particle samples often cluster towards the tails of the posterior probability distribution. This characteristic introduces a degree of randomness in particle selection, thereby impacting the accuracy and real-time efficacy of the observation algorithm. To address this limitation, the approach in this study integrates the Extended Kalman Filter (EKF) to formulate the importance density function of the PF. This integration serves to mitigate linearization errors inherent in nonlinear filtering processes. By assimilating the most recent observation data into the importance density function, the method approximates the posterior probability distribution of the actual state more effectively, consequently enhancing the observational process's accuracy and real-time performance [20–23].

The vehicle state parameters to be observed include the longitudinal velocity u, the lateral velocity v, the yaw rate γ, and lateral force of each electric wheel F_{yij}. The state vector is defined as:

$$\boldsymbol{x} = \left(u, v, \gamma, F_{y10}, F_{y11}, \ldots, F_{yn0}, F_{yn1}\right)^{\mathrm{T}} \tag{53}$$

According to the differential equation of rotational motion of the electric wheel described in Eq. (31), the longitudinal force of the tire can be expressed as:

$$F_{xij} = \frac{1}{R}T_{mij} - \frac{I_{\mathrm{w}}}{R}\dot{\omega}_{ij} \tag{54}$$

The input vector is defined as:

$$\boldsymbol{u} = \left(\delta_1, \dots, \delta_n, F_{x10}, F_{x11}, \dots, F_{xn0}, F_{xn1}\right)^{\mathrm{T}} \tag{55}$$

Based on the recursive equation of the nonlinear state observation model, the current state vector and the input vector can be used to predict the state vector at the next moment. The state recursive equation is derived from the dynamics equations governing the planar motion of the vehicle in Eqs. (15–17).

$$\dot{\boldsymbol{x}}(t) = \tilde{f}(\boldsymbol{x}(t), \boldsymbol{u}(t)) \tag{56}$$

where the prediction of lateral tire forces F_{yij} involves the dynamic magic formula as follows:

$$\dot{F}_{yij} = \frac{C_{l0}}{C_{y0}}u\left(F_{yij\_\mathrm{MF}} - F_{yij}\right) \tag{57}$$

where C_{y0} is the initial lateral deflection stiffness and C_{l0} is the initial lateral displacement stiffness of the tire.

The measurement vector consists of the measured value of the inertial sensor and the rotational speed of each electric wheel. The measurement vector is defined as:

$$\boldsymbol{y} = \left(a_x, a_y, \gamma, \omega_{10}, \omega_{11}, \dots, \omega_{n0}, \omega_{n1}\right)^{\mathrm{T}} \tag{58}$$

According to the principles of tire magic model, when the longitudinal force of the tire does not exceed 80% of the maximum adhesion force that the road can provide, the longitudinal tire slip rate is proportional to the longitudinal force of the tire. Therefore, under normal driving conditions, the measured value of wheel rotational speed can be expressed as:

$$\omega_{ij} \doteq \frac{\left(1 - F_{xij}/k_{s0}\right)}{R}v_{xij} \tag{59}$$

where k_{s0} is the initial longitudinal slip stiffness of the tire. Based on this assumption and the dynamics equations of the planar motion in Eqs. (15–17), the measurement equation can be derived.

$$\boldsymbol{y}(t) = \tilde{h}(\boldsymbol{x}(t), \boldsymbol{u}(t)) \tag{60}$$

The state recursive Eq. (56) and the measurement Eq. (60) form a nonlinear state observation model. The observation of the state parameters of this nonlinear state observation model using EKF–PF is divided into the following steps, with detailed derivation provided in Ref. [24].

(1) Discretization of the state recursive equation and the measurement equation. The discretized equations are expressed as follows:

$$\boldsymbol{x}_{k+1} = f\left(\boldsymbol{x}_k, \boldsymbol{u}_k\right) + \boldsymbol{w}_k (k \in N) \tag{61}$$

$$\boldsymbol{y}_k = h\left(\boldsymbol{x}_k, \boldsymbol{u}_k\right) + \boldsymbol{e}_k (k \in N) \tag{62}$$

where $\boldsymbol{x}_k$ and $\boldsymbol{y}_k$ are the state vector and the observation vector at moment k, respectively, $\boldsymbol{w}_k$ and $\boldsymbol{e}_k$ are the process noise and measurement noise with covariance $\boldsymbol{Q}$ and $\boldsymbol{R}$, respectively.

Since the EKF-PF method uses the EKF algorithm as the proposed distribution, the EKF algorithm needs to be used to update the particles at each state point. The nonlinear functions $f\left(\boldsymbol{x}_k, \boldsymbol{u}_k\right)$ and $h\left(\boldsymbol{x}_k, \boldsymbol{u}_k\right)$ are subjected to a first-order Taylor expansion around the filtered values, resulting in:

$$\boldsymbol{A}_k = \left.\frac{\partial f}{\partial x}\right|_{x=\hat{x}_k} \tag{63}$$

$$\boldsymbol{C}_k = \left.\frac{\partial h}{\partial x}\right|_{x=\hat{x}_k} \tag{64}$$

Then the discretized observation model can be expressed as:

$$\boldsymbol{x}_{k+1} = \boldsymbol{A}_k\boldsymbol{x}_k + \boldsymbol{B}_k\boldsymbol{u}_k + \boldsymbol{w}_k \tag{65}$$

$$\boldsymbol{y}_k = \boldsymbol{C}_k\boldsymbol{x}_k + \boldsymbol{D}_k\boldsymbol{u}_k + \boldsymbol{e}_k \tag{66}$$

(2) Particle initialization. The particles $\left\{\boldsymbol{x}_0^i\right\}_{i=1}^N$ is generated from the prior probability $p\left(x_0\right)$, the weights of all particles are initially set to $1/N$, and the initial covariance is $\hat{P}_0^i = \mathrm{var}\left(x_0\right)$.

(3) Update the particles using EKF. The predicted value $\hat{\boldsymbol{x}}_{k|k-1}^i$ for the next moment of the system state is calculated based on the filtered value $\hat{\boldsymbol{x}}_{k-1|k-1}^i$ of the system at the previous moment.

$$\hat{\boldsymbol{x}}_{k|k-1}^i = \boldsymbol{A}_{k-1}\hat{\boldsymbol{x}}_{k-1|k-1}^i + \boldsymbol{B}_{k-1}\boldsymbol{u}_{k-1} \tag{67}$$

Then the predicted value of the error covariance matrix is calculated at the next moment and the Kalman gain matrix.

$$\boldsymbol{P}_{k|k-1}^i = \boldsymbol{A}_{k-1}\boldsymbol{P}_{k-1|k-1}^i\boldsymbol{A}_{k-1}^{\mathrm{T}} + \boldsymbol{Q}_{k-1} \tag{68}$$

$$\boldsymbol{K}_k = \boldsymbol{P}^i_{k|k-1}\boldsymbol{C}_k^{\mathrm{T}}\left(\boldsymbol{C}_k\boldsymbol{P}^i_{k|k-1}\boldsymbol{C}_k^{\mathrm{T}} + \boldsymbol{R}_k\right)^{-1} \tag{69}$$

Based on the calculated Kalman gain matrix, combining the predicted and latest observed values of the system, the filtered values of the system for the next moment can be derived as:

$$\hat{\boldsymbol{x}}^i_{k|k} = \hat{\boldsymbol{x}}^i_{k|k-1} + \boldsymbol{K}_k\left[\boldsymbol{y}_k - h\left(\hat{\boldsymbol{x}}^i_{k|k-1}, \boldsymbol{u}_k\right)\right] \tag{70}$$

Update the error covariance matrix and update particles.

$$\boldsymbol{P}^i_{k|k} = \left(\boldsymbol{I} - \boldsymbol{K}_k\boldsymbol{C}_k\right)\boldsymbol{P}^i_{k|k-1} \tag{71}$$

$$\boldsymbol{x}^i_k \sim q\left(\hat{\boldsymbol{x}}^i_k \middle| \boldsymbol{x}^i_{k-1}, \boldsymbol{y}_k\right) = N\left(\hat{\boldsymbol{x}}^i_k, \boldsymbol{P}^i_k\right) \tag{72}$$

(4) Calculate and normalize particle weights.

$$\hat{w}^i_k \propto \frac{p\left(\boldsymbol{y}_k \middle| \hat{\boldsymbol{x}}^i_k\right) p\left(\hat{\boldsymbol{x}}^i_k \middle| \hat{\boldsymbol{x}}^i_{k-1}\right)}{q\left(\hat{\boldsymbol{x}}^i_k \middle| \hat{\boldsymbol{x}}^i_{k-1}, y_{1:k}\right)} \tag{73}$$

$$\tilde{w}^i_k = \hat{w}^i_k\left(\sum_{i=1}^{N}\hat{w}^i_k\right)^{-1} \tag{74}$$

(5) Resampling. To solve the problem of particle degradation and avoid devoting too much computing time to particles with smaller weights, a resampling step is introduced to calculate the effective particle number N_e, compare N_e with a preset threshold, and determine whether resampling is needed.

$$N_e = \left[\sum_{i=1}^{N}\left(\hat{w}^i_k\right)^2\right]^{-1} \tag{75}$$

(6) State vector estimation.

$$\hat{\boldsymbol{x}}^i_k = \sum_{i=1}^{N}\tilde{w}^i_k\boldsymbol{x}^i_k \tag{76}$$

3.2.2 Transient Steering Center Distance Calculation

As introduced in Sect. 2, the transient steering center position determines the relationship between the first axle steering angle (or steering wheel steering angle) and the steering angle target of each other axle, as described in Eqs. (22–24). The transient steering center position is not a constant value during actual vehicle driving and will varies with vehicle parameters such as vehicle velocity. To ensure smooth steering control and minimize tire wear, the transient steering center distance x_{cs} needs to be calculated.

The parameter K_n is the equivalent stability coefficient of an n-axle vehicle, which is greater than 0 when the vehicle is understeering, taking on values greater than 0 for understeering conditions, equal to 0 for neutral steering, and less than 0 for oversteering scenarios. Vehicles with oversteering characteristics might be destabilized if the velocity reaches or exceeds a critical velocity, and vehicles in general need to have certain understeering characteristics. B_n is the equivalent coefficient of sideslip angle for the n-axis vehicle.

This paper adopts the transient parameters calculation methodology proposed in Ref. [25], which involves analyzing the linear 2- DOF state equation of multi-axle vehicles. Assuming that the effect of rolling motion is neglected and that all tires have the same lateral deflection stiffness C_y (which is negative), K_n, B_n, and x_{cs} are given by:

$$B_n = \frac{\left(\sum_{i=1}^{n} x_i - nx_{cs0}\right)\left(\sum_{i=1}^{n} m_{\mathrm{b}i}x_i\right) - \left(\sum_{i=1}^{n} x_i^2 - x_{cs0}\sum_{i=1}^{n} x_i\right)\left(\sum_{i=1}^{n} m_{\mathrm{b}i} + m_{\mathrm{a}}\right)}{2C_y\left[\left(\sum_{i=1}^{n} x_i\right)^2 - n\sum_{i=1}^{n} x_i^2\right]} \tag{77}$$

$$K_n = \frac{n\left(\sum_{i=1}^{n} m_{\mathrm{b}i}x_i\right) - \left(\sum_{i=1}^{n} x_i\right)\left(\sum_{i=1}^{n} m_{\mathrm{b}i} + m_{\mathrm{a}}\right)}{2C_y\left[\left(\sum_{i=1}^{n} x_i\right)\left(1 + \sum_{i=2}^{n} h_i\right) - n\left(x_1 + \sum_{i=2}^{n} x_ih_i\right)\right]} \tag{78}$$

$$x_{cs} = x_{cs0} - B_nu^2 \tag{79}$$

where x_{cs0} is the initial steering center distance, namely the value when the vehicle is steering in place.

The curves of the equivalent stability coefficient K_n and the transient steering center distance x_{cs} with vehicle velocity u are depicted in Fig. 9. As can be seen from Fig. 9(a), with the increase in velocity, K_n gradually decreases, that is, the degree of understeering decreases. Notably, when the vehicle speed surpasses the critical threshold denoted by the red marker in the figure, the vehicle transitions into an oversteering state. Oversteering conditions, particularly at high speeds, can compromise maneuvering stability, necessitating consideration in the vehicle's steering control strategy. From Fig. 9(b), it can be seen that as the vehicle velocity increases, the transient steering center distance is accelerating forward. At high speeds, the transient steering center will move to the front of CG or even the first axle, as highlighted by the red marker. Such displacement can lead to severe vehicle instabilities like tailing, aligning with the observations derived from the analysis of Fig. 9(a).

3.3 Lower Controller

3.3.1 EMPS Controller

The EMPS controller receives inputs from various sources, including the state parameters estimated by the upper controller, the target steering angles for each electric

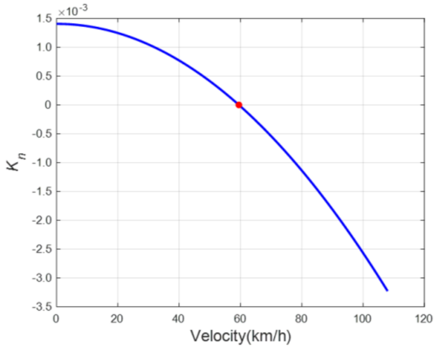

(a) Curve of equivalent stability coefficient with velocity

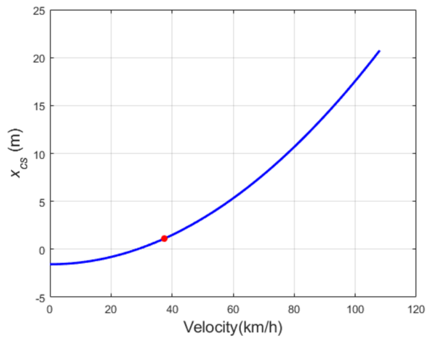

(b) Curve of transient steering center distance with velocity

Fig. 9 Vehicle transient steering characteristics curves

drive axle (determined using Eqs. (22–24) incorporating the calculated transient steering center distance), and the real-time steering angles recorded by sensors. Leveraging this information, the EMPS controller derives and outputs the demanded differential torque $\Delta T_{mi-EMPS}$ utilizing the sliding mode control (SMC) method. Given the substantial nonlinearity inherent in the steering dynamics model, SMC emerges as a pivotal tool for controlling nonlinear systems. SMC offers distinct advantages such as a straightforward control system algorithm, rapid response times, and robust performance [26, 27].

Define the following sliding surface, considering the axle steering angle tracking error and its difference value.

$$S_\delta = \delta_{id} - \delta_i + \lambda_\delta\left(\dot{\delta}_{id} - \dot{\delta}_i\right) \tag{80}$$

where δ_{id} is the desired axle steering angle and λ_δ is the difference value coefficient. Substitute Eq. (47) into Eq. (80).

$$\begin{aligned}\dot{S}_\delta &= \dot{\delta}_{id} - \dot{\delta}_i + \lambda_\delta \ddot{\delta}_{id} - \lambda_\delta \ddot{\delta}_i \\ &= \dot{\delta}_{id} - \dot{\delta}_i + \lambda_\delta \ddot{\delta}_{id} - \frac{\lambda_\delta}{I_{si}}\left(M_i - M_{ayi} - M_{ati} - K_p\delta_i - C_p\dot{\delta}_i - M_{fi}\right)\end{aligned} \tag{81}$$

Using the exponential convergence law, so that

$$\dot{S}_\delta = -\varepsilon_\delta \mathrm{sgn}\left(S_\delta\right) - k_\delta S_\delta \tag{82}$$

where $\mathrm{sgn}\left(S_\delta\right)$ is the sign function. Define the lyapunov function as follows:

$$V_\delta = \frac{1}{2}S_\delta^2 \tag{83}$$

Then,

$$\dot{V}_\delta = S_\delta\dot{S}_\delta = -\varepsilon_\delta S_\delta \mathrm{sgn}\left(S_\delta\right) - k_\delta S_\delta^2 = -\varepsilon_\delta\left|S_\delta\right| - k_\delta S_\delta^2 \tag{84}$$

As long as ε_δ and k_δ are chosen to be positive values, it is guaranteed that V_δ and S_δ converges exponentially to 0 and the convergence rate depends on k_δ.

Considering steering friction moment as a disturbance, substituting Eq. (81) into Eq. (82) gives the EMPS axle steering angle tracking control law given as follows. To mitigate the control law jitter, the sign function $\mathrm{sgn}\left(S_\delta\right)$ is replaced by the saturation function $\mathrm{sat}\left(S_\delta\right)$.

$$\begin{aligned}M_i =& \frac{I_{si}}{\lambda_\delta}\left[\dot{\delta}_{id} - \dot{\delta}_i + \lambda_\delta \ddot{\delta}_{id} + \varepsilon \mathrm{sgn}\left(S_\delta\right) + kS_\delta\right] \\ &+ M_{ayi} + M_{ati} + K_p\delta_i + C_p\dot{\delta}_i\end{aligned} \tag{85}$$

$$\mathrm{sat}\left(S_\delta\right) = \begin{cases} 1, \ S_\delta \geq \xi \\ \frac{S_\delta}{\xi}, \ -\xi < S_\delta < \xi \\ -1, \ S_\delta \leq -\xi \end{cases} \tag{86}$$

where ξ is the parameter that affects the degree of jitter, when ξ is infinitesimal, $\mathrm{sat}\left(S_\delta\right)$ turns into a saturation function.

Combining with Eqs. (48)-(49), the differential torque required by the i-th axle is expressed as:

$$\Delta T_{mi-EMPS} = M_i / \left(\frac{R_x}{R}\cos\tau\cos\sigma + \sin\sigma\right) \tag{87}$$

The EMPS steering control mode is shown in Fig. 10, where the steering angle tracking of each axle is achieved by the differential torque independently or optionally with a mechanical steering system.

3.3.2 DYC Controller

The electronic differential torque of the EMPS introduces an additional vehicle yaw moment, which impacts vehicle stability, especially during high-speed steering on roads with low adhesion. This additional yaw moment may aggravate the tendency of vehicle destabilization, necessitating the intervention of the stability control system in situations where the vehicle is operating at its limits. In this paper, the DYC method is adopted for

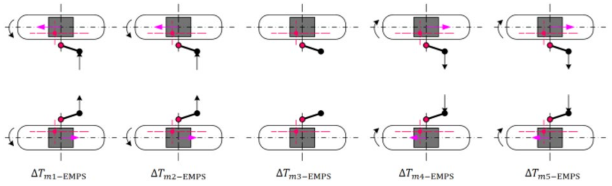

Fig. 10 EMPS steering control mode

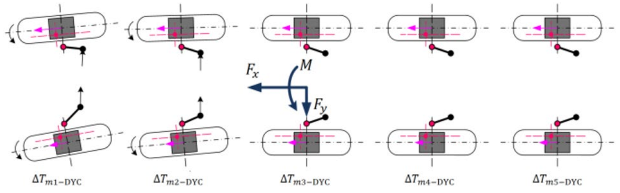

Fig. 11 DYC stability control mode

stability control. The DYC system in multi-axle distributed drive vehicles has two major advantages. Firstly, it enables optimal control of the electric wheels due to the precise and rapid response of the in-wheel motor control. Secondly, it allows the vehicle to achieve the desired yaw moment through torque distribution of the electric wheels, eliminating the need for intervention from the braking system and minimizing power loss.

The DYC controller takes input from the vehicle's state parameters provided by the upper controller. It then adjusts the torques of the electric wheels to generate the target yaw moment, ensuring that the current vehicle yaw rate follows the calculated target value as per Eq. (26). The SMC method, similar to that of the EMPS controller, is used for yaw rate tracking control. By considering the tracking error and its integral, a sliding surface is defined as:

$$S_z = \gamma_{\mathrm{d}} - \gamma + \lambda_z \int_0^t \left(\gamma_{\mathrm{d}} - \gamma\right)\mathrm{d}t \tag{88}$$

where λ_z is the integral value coefficient, and γ_{d} is the desired value of yaw rate.

Similarly, by employing the exponential convergence law and adopting a methodology akin to defining the Lyapunov function $V_z = \frac{1}{2}S_z^2$, the control law for DYC yaw rate tracking can be deduced as follows:

$$M_z = I_z\left[\dot{\gamma}_{\mathrm{d}} + \lambda_z\left(\gamma_{\mathrm{d}} - \gamma\right) + \varepsilon_z \mathrm{sat}\left(S_z\right) + k_z S_z\right] \tag{89}$$

The contribution of the differential torque $\Delta T_{mi\_\mathrm{DYC}}$ of the i-th axle to the vehicle yaw moment is expressed as:

$$M_{zi} = F_{xi}\sin\delta_i\left(x_i - x_{cs}\right) + \frac{b_{\mathrm{w}}}{R}\cos\delta_i \Delta T_{mi\_\mathrm{DYC}} \tag{90}$$

Due to the different tire loads of different electric wheels, the saturation torque available for each wheel is also different. Thus, in order to obtain better directional stability and steering control capability, this paper uses the optimal control allocation to generate the target differential torque ΔT_{mi_DYC} for each axle, considering minimization of the tires' utilization adhesion coefficient.

$$\left\{ \Delta T_{mi\_\mathrm{DYC}},\ i = 1 \sim n \right\} = \arg \min_{\left\{\Delta T_{mi\_\mathrm{DYC}}\right\}} \sum_{i=1}^{n} \left| \frac{\Delta T_{mi\_\mathrm{DYC}}}{\sum_{j=0,1} F_{zij}} \right|$$
$$\text{s.t.} \sum_{i=1}^{n} M_{zi} = M_z \tag{91}$$

The DYC stability control mode is shown in Fig. 11, where the steering angle of each axle is mainly executed by the mechanical steering system, while the electronic differential torque is only employed to generate the yaw moment to track the target yaw rate. Notably, for enhanced stability during high-speed maneuvers, certain axles within the steering system may be locked with their steering angles set to 0. This configuration allows the differential torque of each electric drive axle to generate the required yaw moment, ensuring that the vehicle maintains its tracking of the target yaw rate and thereby preserving yaw stability.

3.3.3 Composite Steering Controller Weight Assignment Module

Based on the controller design and analysis above, it is noted that both the EMPS and DYC controllers share the same control objective, which is the differential torque management of each electric drive axle. However, their respective applicable working conditions differ. The EMPS controller is suitable for steering assistance during low-speed and steady-state maneuvers, whereas the DYC controller is designed for high-speed vehicle stability control. In order to ensure accurate and smooth switching of the two control subsystems when the stability state of the vehicle changes, the composite steering controller weight assignment module is designed considering multiple judgment dimensions.

3.3.3.1 Equivalent Stability Coefficient Judgment

From Fig. 9, it can be seen that as the speed increases, K_n gradually decreases and the transient steering center position shifts forward, leading to the instability of the vehicle steering system at high speeds.

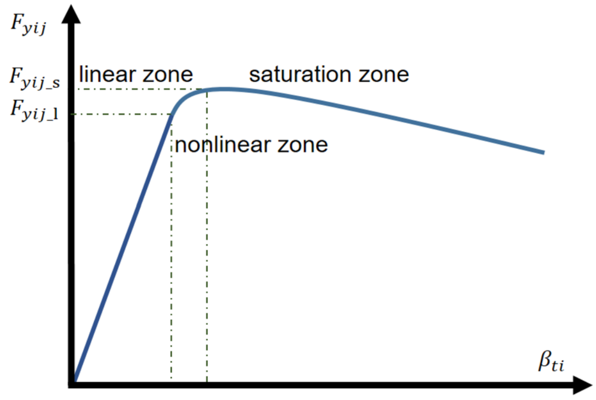

Fig. 12 Tire lateral force characteristic curve

According to Eqs. (77)-(79), when the relevant vehicle parameters are known, calculate vehicle speed u_{th1} such that $K_n = 0$, and u_{th2} such that $x_{cs} = x_1$. The vehicle speed boundary of the unstable domain determined by the vehicle steering characteristics is:

$$u_{\text{th}} = \min \left\{ u_{\text{th1}} \quad u_{\text{th2}} \right\} \tag{92}$$

3.3.3.2 Tire Lateral Force Judgment

EMPS controller leads to a large tire lateral force for each electric wheel, which may cause the tire to approach the adhesion limit. Based on the accurate estimation of the tire lateral force F_{yij} for each electric wheel in upper controller, the tire lateral force can be used to determine whether the tires are within a stable steering domain.

According to the tire force characteristics introduced in Sect. 2.3, the tire force can be divided into three regions: linear region, non-linear region, and saturation region. Taking the tire lateral force characteristic curve as an example, as shown in Fig. 12: In the linear zone, the relationship between tire sideslip angle and lateral force is nearly linear, enabling the tire to supply adequate lateral force for the vehicle within this range. In the nonlinear zone, the tire sideslip angle and lateral force show an obvious nonlinear relationship. Although the lateral force can still respond to changes in tire sideslip angle, the change amplitude is not as obvious as in the linear zone. In the saturation zone, the tire lateral force is less sensitive to the change in tire sideslip angle, and for some tires, there may even be a negative response, leading to an insufficient provision of lateral force for the vehicle. The characteristics of tire lateral force play a crucial role in the lateral stability of the vehicle. Therefore, studying the operational zone reached by the tire lateral force allows for the evaluation of the vehicle's stability.

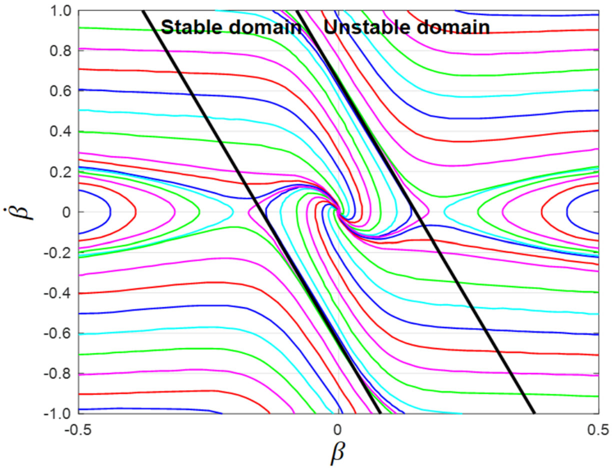

Fig. 13 The $\beta - \dot{\beta}$ phase plane diagram

The lateral force boundary of the tire F_{yij_s} between the nonlinear zone and the saturation zone is obtained directly and precisely from the extreme value point of the lateral force by the magic formula Eq. (36).

$$F_{yij\_s} = \max_{\alpha_{ij}} F_{yij\_MF} \tag{93}$$

3.3.3.3 Phase Plane Method Judgment

Given the values of the longitudinal vehicle speed u and the first axle steering angle δ_1, and then given different initial values of the sideslip angle β, the $\beta - \dot{\beta}$ phase plane diagram for different longitudinal vehicle speeds and steering angles can be plotted according to the theory of phase planes. There is a dense band area of trajectory lines in the phase plane, and all the state points in this area will return to the coordinate origin after a certain time, which is called the stable equilibrium point of the phase plane, while the state points outside this area cannot return to the stable equilibrium

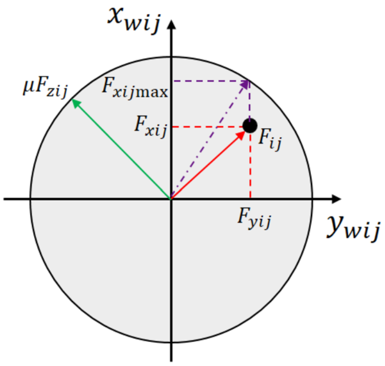

Fig. 14 The friction circle of the electric wheel tire

Table 1 Main parameters of the simulated vehicle

Parameter	Symbol	Unit	Value
Sprung mass	m_a	kg	4457
Unsprung mass	$m_{bi}(i = 1 \sim 4)$	kg	275,275,785,785
Yaw inertia	I_z	kg·m^2	34,693.7
Tire radius	R	m	0.51
Wheel rotational inertia	I_{w}	kg·m^2	14
Vehicle track	b_w	m	2.07
Height of CG	h_{cg}	m	1.17
Initial steering center distance	x_{cs0}	m	-1.57
Distance to the first axle	$L_2, L_3, L_4, L_{\mathrm{CG}}$	m	1.81,6.00,7.81,1.11
Caster angle of the kingpin	τ	deg	5.2
Lateral inclination of the kingpin	σ	deg	4.9
Kingpin lateral offset	R_x	mm	9.8
Pneumatic trail	R_y	mm	43.7

point. This area is called the stable domain of the phase plane, as shown in Fig. 13.

The conclusion of Ref. [28] elaborates that the boundary of the stable domain in the $\beta - \dot{\beta}$ phase plane is mainly influenced by the tire-road attachment coefficient, with comparatively minor influence from longitudinal speed and steering angle. Therefore, the stable domain boundary of the $\beta - \dot{\beta}$ phase plane is relatively simpler to identify and is chosen as the basis of the working conditions judgment. The boundary of the $\beta - \dot{\beta}$ phase plane domain can be represented by the following equation:

$$\left|\dot{\beta} + k_{\beta 1}\beta\right| \leq k_{\beta 2} \tag{94}$$

where $k_{\beta 1}$ and $k_{\beta 2}$ are the stable domain boundary coefficients, related to the pavement adhesion coefficient μ, and can be determined experimentally or by empirical equations. The distances from the working points in the phase plane to the centerline and boundary of the stable zone are as follows:

$$d_\beta = \frac{\left|\dot{\beta} + k_{\beta 1}\beta\right|}{\sqrt{1 + k_{\beta 1}^2}} \tag{95}$$

$$d_{\beta\_\mathrm{s}} = \frac{\left|k_{\beta 2}\right|}{\sqrt{1 + k_{\beta 1}^2}} \tag{96}$$

To assign the control weights of EMPS and DYC controllers, the control weights of EMPS controller calculated based on the above three vehicle stability judgments are defined as k_{EMPS_u}, k_{EMPS_y}, and k_{EMPS_β}, respectively. Considering the smooth switching between controllers, on the basis of the judgment of each boundary of the unstable domain, the boundaries of the stable zone and the transition zone are defined as follows:

$$u_{\mathrm{th}\_1} = \kappa_u u_{\mathrm{th}s} \tag{97}$$

$$F_{yij\_1} = \kappa_y F_{yij\_\mathrm{s}} \tag{98}$$

$$d_{\beta\_1} = \kappa_\beta d_{\beta\_\mathrm{s}} \tag{99}$$

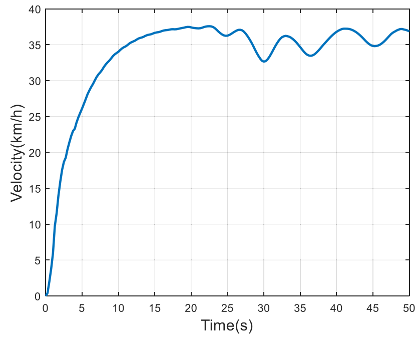

(a) Vehicle velocity

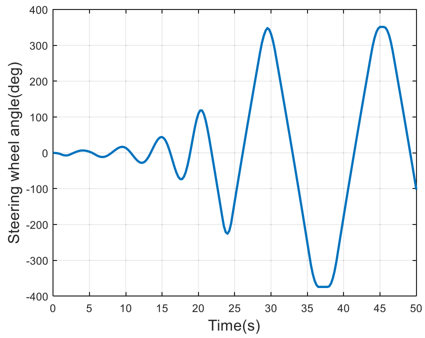

(b) Steering wheel angle

Fig. 15 EMPS simulation working conditions

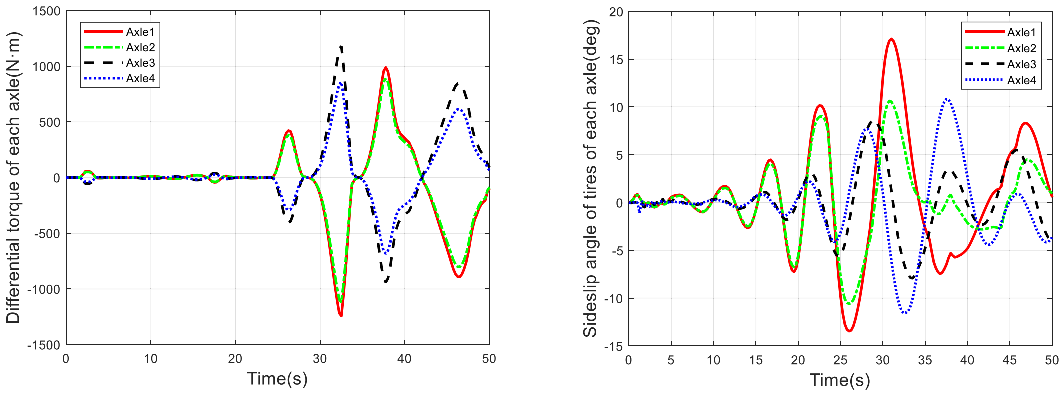

(a) Differential torque of each axle

(d) Sideslip angle of tires of each axle

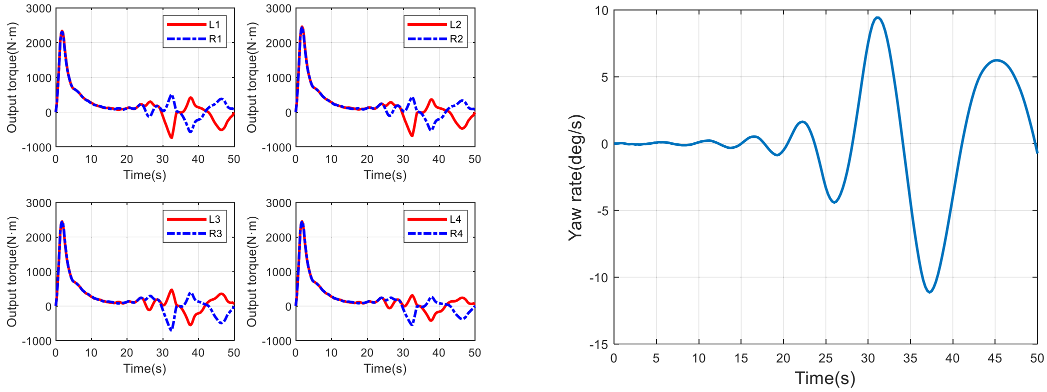

(b) Output torque of each electric wheel

(e) Vehicle yaw rate

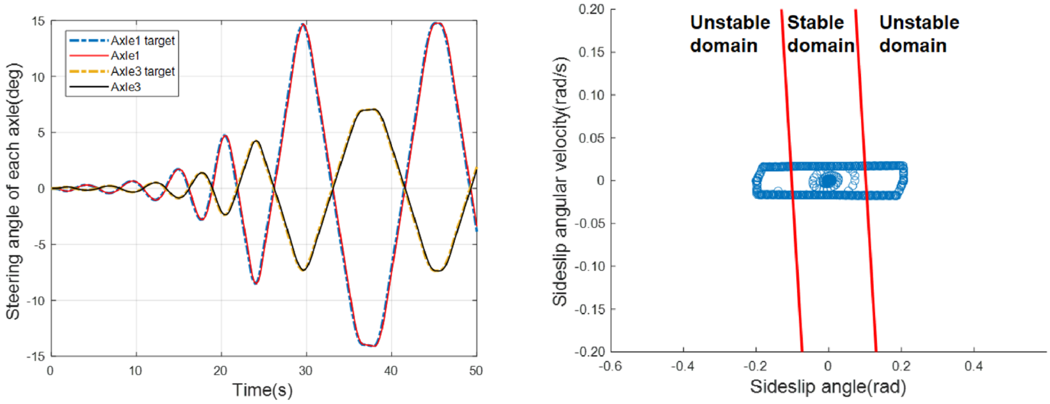

(c) Steering angle of axle 1&3

(f) $\beta - \dot{\beta}$ trajectory

Fig. 16 EMPS simulation results

where κ_u, κ_y, and κ_β are the transition zone boundary coefficients, determined according to the empirical formula or test calibration, and taking the value of $0 \sim 1$.

In summary, the vehicle operates in a stable state where the impact of EMPS does not pose a risk of handling instability. Therefore, there is no imminent danger of destabilization, and intervention by the DYC controller is unnecessary. On the contrary, in the non-stable zone, the vehicle state is deemed unstable, prompting the deactivation of EMPS and the activation of DYC for stability control to ensure the vehicle's stability. The transition zone is used to prevent sudden changes

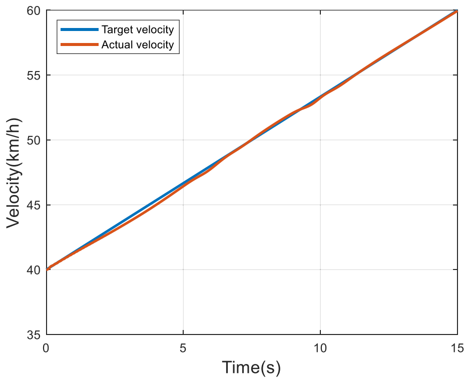

(a) Vehicle velocity

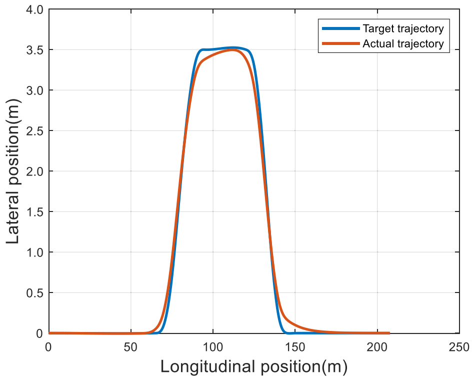

(b) Vehicle trajectory

Fig. 17 Double lane-change simulation conditions

in control torque by blending and weighting the differential torque outputs of both EMPS and DYC.

$$k_{\mathrm{EMPS\_}u} = \begin{cases} 1,\ u \le u_{\mathrm{th\_l}} \\ \frac{u_{\mathrm{th}}-u}{u_{\mathrm{th}}-u_{\mathrm{th\_l}}},\ u_{\mathrm{th}} \ge u > u_{\mathrm{th\_l}} \\ 0,\ u > u_{\mathrm{th}} \end{cases} \tag{100}$$

$$k_{\mathrm{EMPS\_}y} = \begin{cases} 1,\ \max\limits_{i,j}\left\{\frac{F_{yij}}{F_{yij\_s}}\right\} \le \kappa_y \\ \frac{1-\max\limits_{i,j}\left\{\frac{F_{yij}}{F_{yij\_s}}\right\}}{1-\kappa_y},\ 1 \ge \max\limits_{i,j}\left\{\frac{F_{yij}}{F_{yij\_s}}\right\} > \kappa_y \\ 0,\ \max\limits_{i,j}\left\{\frac{F_{yij}}{F_{yij\_s}}\right\} > 1 \end{cases} \tag{101}$$

$$k_{\mathrm{EMPS\_}\beta} = \begin{cases} 1,\ d_\beta \le d_{\beta\_l} \\ \frac{d_{\beta\_s}-d_\beta}{d_{\beta\_s}-d_{\beta\_l}},\ d_{\beta\_s} \ge d_\beta > d_{\beta\_l} \\ 0,\ d_\beta > d_{\beta\_s} \end{cases} \tag{102}$$

The calculated weights of the EMPS and DYC controllers and the differential torque required by the ith axle is expressed as follows:

$$k_{\mathrm{EMPS}} = k_{\mathrm{EMPS\_}u} k_{\mathrm{EMPS\_}y} k_{\mathrm{EMPS\_}\beta} \tag{103}$$

$$k_{\mathrm{DYC}} = 1 - k_{\mathrm{EMPS}} \tag{104}$$

$$\Delta T_{mi} = k_{\mathrm{EMPS}} \Delta T_{mi\mathrm{\_EMPS}} + k_{\mathrm{DYC}} \Delta T_{mi\mathrm{\_DYC}} \tag{105}$$

3.3.4 Torque Constraint Module

According to Eq. (105), the target torque output of each electric wheel is:

$$T_{mij\mathrm{\_tar}} = T_{mi\mathrm{\_tar}} - \frac{(-1)^j}{2} \Delta T_{mi} \tag{106}$$

where $T_{mi\mathrm{\_tar}}$ is the target total torque output of the ith axle. The distribution of torque between axles is not discussed in this paper. Considering the torque characteristics of the in-wheel motor, and the friction circle of the electric wheel tire (as in Fig. 14), the target output torque needs to be constrained to avoid the target torque not being output properly as expected or the tires slipping.

The constraint set according to the friction circle and the current maximum torque of the motor derived from the torque characteristics and the current rotational speed is as follows:

$$\left|T_{mij\mathrm{\_tar}}\right| \le \min\left\{ R\sqrt{\mu^2 F_{zij}^2 - F_{yij}^2}\ \ T_{mij\max}\left(\omega_{ij}\right) \right\} \tag{107}$$

Torque offset calculated from the constraint is:

$$T_{mij\mathrm{\_ost}} = \max\left\{ \left[\left|T_{mij\mathrm{\_tar}}\right| - \min\left\{ R\sqrt{\mu^2 F_{zij}^2 - F_{yij}^2}\ \ T_{mij\max}\left(\omega_{ij}\right) \right\}\right]\ 0 \right\} \left[-\mathrm{sgn}\left(T_{mij\mathrm{\_tar}}\right)\right] \tag{108}$$

In order to ensure that the differential torques can meet the steering control requirements, the torque constraint module simultaneously adjusts the target output torques of the wheels on both sides of the same axle equally.

$$T_{mi\mathrm{\_ost}} = \max_{j=0,1}\left\{\left|T_{mij\mathrm{\_ost}}\right|\right\} \mathrm{sgn}\left(T_{mi0\mathrm{\_ost}}\right) \tag{109}$$

The final target output torque command for each electric wheel is as follows:

$$T_{mij\mathrm{\_tar}}^{*} = T_{mij\mathrm{\_tar}} + T_{mi\mathrm{\_ost}} \tag{110}$$

Fig. 18 DYC simulation results

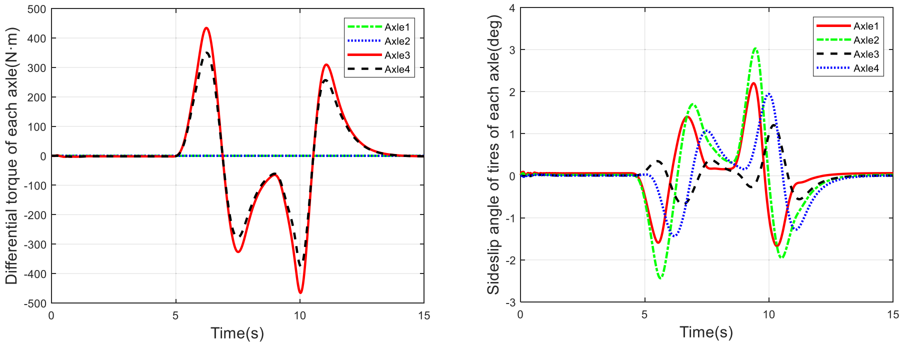

(a) Differential torque of each axle

(d) Sideslip angle of tires of each axle

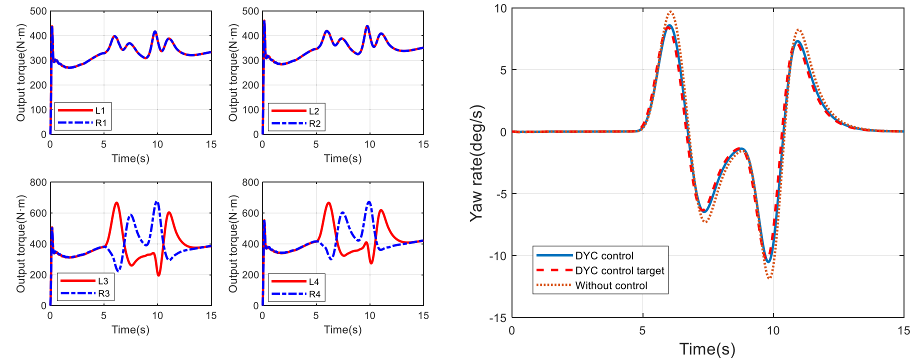

(b) Output torque of each electric wheel

(e) Vehicle yaw rate

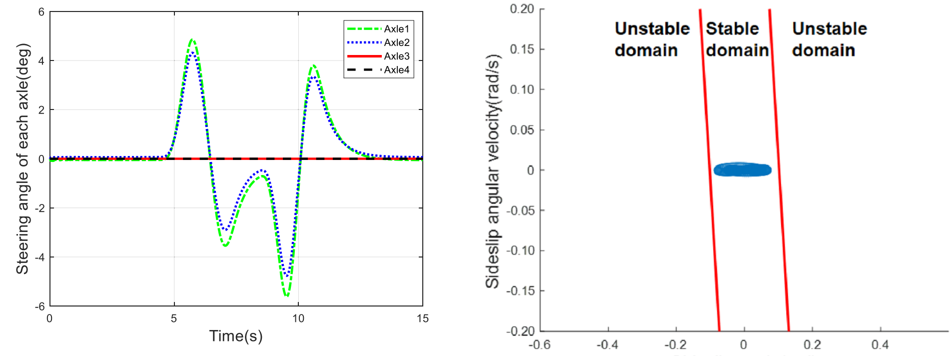

(c) Steering angle of each axle

(f) $\beta - \dot{\beta}$ trajectory

4 Simulation and Experimentation

4.1 Simulation and Analyses

4.1.1 Simulation of EMPS Control Mode

To assess the efficacy of the composite steering control strategy for multi-axle distributed drive vehicles, a co-simulation model was developed using the MATLAB/Simulink and TruckSim. The simulation focuses on a four-axle vehicle with distributed drive, and the key vehicle parameters are outlined in Table 1.

To validate the effectiveness and applicability of EMPS, a simulation is conducted under specific vehicle velocity and steering wheel angle working conditions as depicted in Fig. 15. The velocity rises gradually from 0, and the steering wheel angle changes in a sinusoidal shape with gradually increasing amplitude.

The simulation results encompassing the differential torque of each axle, output torque of each electric wheel, steering angle of each axle, sideslip angle of tires for each axle, vehicle yaw rate, and the $\beta - \dot{\beta}$ trajectory of the vehicle are shown in Fig. 16(a) to (f), respectively. From the results, it can be seen that the EMPS controller effectively tracks

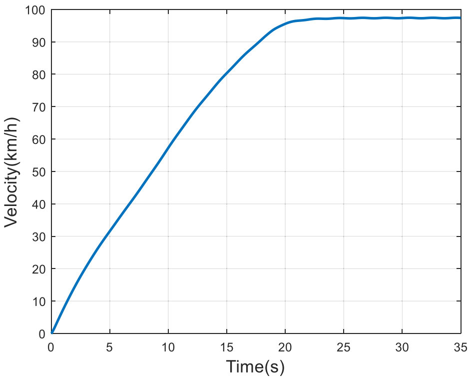

(a) Vehicle velocity

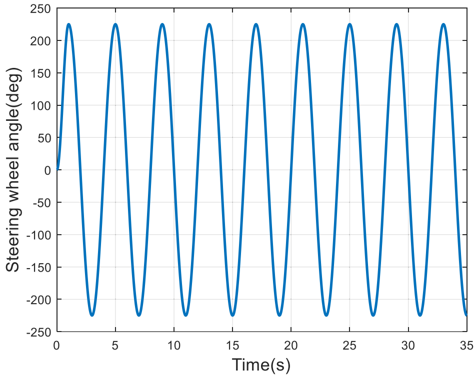

(b) Steering wheel angle

Fig. 19 Composite steering simulation working conditions

the target steering angle for each axle corresponding to the steering wheel angle by generating the target electronic differential torques and distributing them to electric wheels. The steering angles of each axle conforms to Ackermann's steering equation, which can effectively reduce tire wear. The steering angle tracking error remains minimal, with a relative error not exceeding 1.5%, and a tracking time delay of approximately one control step.

The simulation results show that the EMPS controller has the ability to achieve steering maneuvers and improve steering maneuverability only through torque distribution between electric wheels without the intervention of mechanical steering system. However, as the vehicle velocity and steering amplitude increase, the sideslip angle and lateral force of each tire increase accordingly, and the $\beta - \dot{\beta}$ phase plane trajectory gradually moves from the stable zone to the unstable zone. This observation aligns with the research's key assertion that EMPS control is effective within specific operational constraints.

4.1.2 Simulation of DYC Control Mode

A double lane-change simulation is conducted to evaluate the DYC controller, setting the target speed to 40–60 km/h acceleration and the road adhesion coefficient to 0.6. The simulated vehicle velocity and trajectory are illustrated in Fig. 17.

The simulation results are shown in Fig. 18(a) to (f). In this simulation condition, the vehicle operates within the unstable zone and the DYC controller acts to maintain the vehicle yaw stability. From the vehicle trajectory results, it can be seen that the vehicle has sufficient road following ability under DYC control. To mitigate instability risks at high speeds, the controller locks the steering functionality of the two rear axles and generates the vehicle's yaw moment through the differential torques of these axles, as illustrated in Fig. 18(a) to (c).

Since DYC relies mainly on the mechanical steering system to complete the axle steering, and the electronic differential torques are only used to provide the yaw moment, thus each tire has a smaller sideslip angle and a lower risk of instability, as can be seen in Fig. 18(d) compared to Fig. 16(d). The conclusion is also consistent with the analysis in the controller weight assignment module.

Figure 18(e) shows that the yaw moment generated by DYC effectively follows the target yaw rate and effectively reduces the deviation of the yaw rate from the target value in uncontrolled conditions. Figure 18(f) indicates that the $\beta - \dot{\beta}$ trajectory keeps converging within the stability zone under DYC control, which proves that the proposed composite steering control is beneficial to the vehicle stability.

4.1.3 Simulation of Composite Control Mode

In order to verify the control effect of the composite steering controller under different vehicle velocity and steering wheel angle driving maneuvers, a simulation scenario involving gradual vehicle acceleration and sinusoidal steering wheel angle modulation is established. The simulated vehicle velocity and steering wheel angle are shown in Fig. 19.

The simulation results of the composite steering controller are shown in Fig. 20(a) - (i). Figure 20(a) depicts the results of the steering controller weight assignment. In this simulation condition, steering by EMPS controller alone will destabilize the vehicle. The curves of the sub coefficients show that the main influences of the weight assignment in this condition are equivalent stability coefficient and $\beta - \dot{\beta}$ trajectory, while the tire forces always have sufficient margin.

Fig. 20 Composite steering simulation results

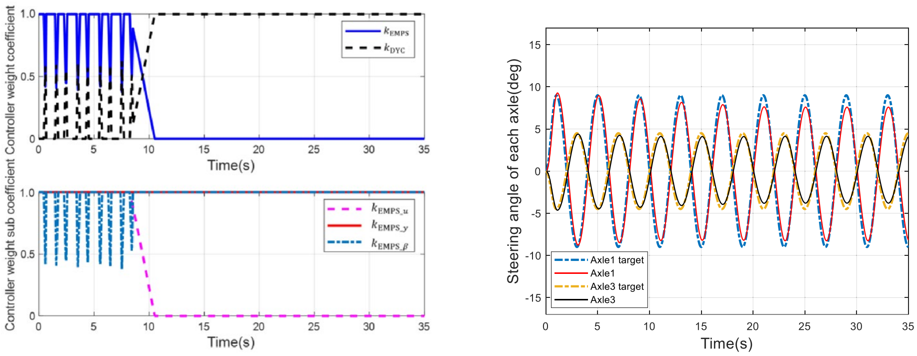

(a) Steering controller weights

(e) Steering angle of axle 1&3

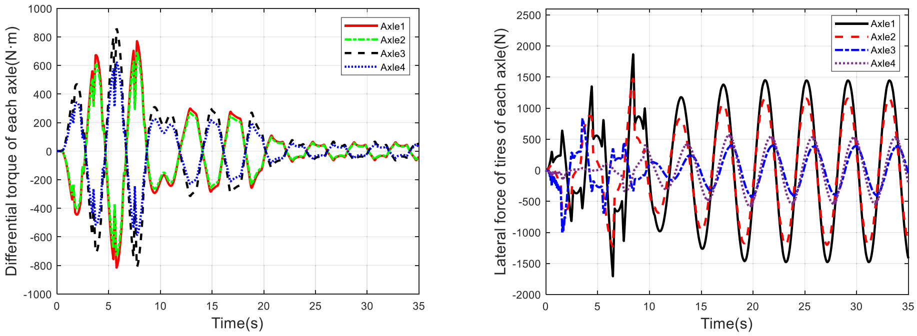

(b) Differential torque of each axle

(f) Lateral tire forces of each axle

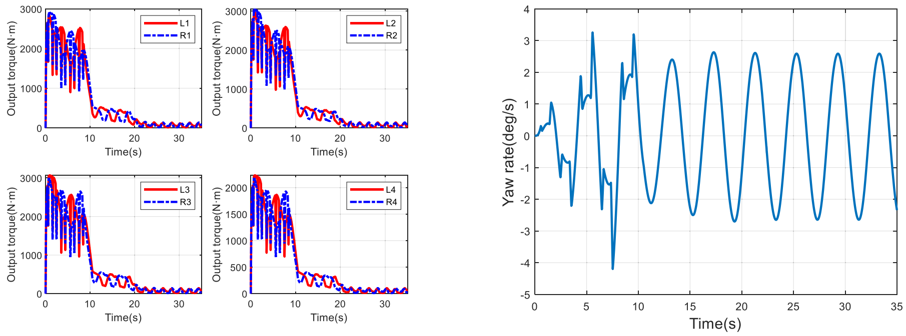

(c) Output torque of each electric wheel

(g) Vehicle yaw rate

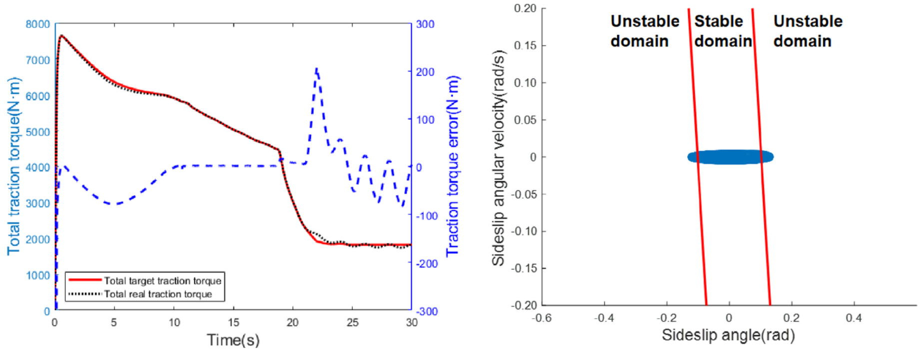

(d) Total traction torque error of electric wheels

(h) $\beta - \dot{\beta}$ trajectory with only EMPS control

Fig. 20 (continued)

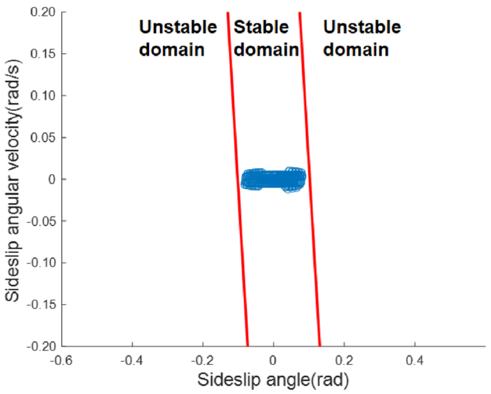

(i) $\beta-\dot{\beta}$ trajectory with composite steering control

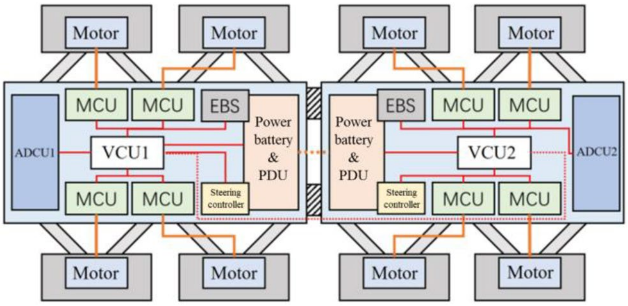

Fig. 21 Test vehicle architecture

(a) Four-axle configuration

(b) Two-axle configuration

Fig. 22 Test vehicle photos

Table 2 Main parameters of the 4×4 test vehicle

Parameter	Unit	Value
Total unloaded mass	kg	320
Unloaded axle load	kg	160,160
Wheelbase	m	0.85
Vehicle track	m	0.95
Maximum speed	km/h	60
Power battery voltage	V	48
Power battery capacity	kW·h	1.38
Power battery power	kW	2.76
Tire specification	–	185/55 R16
Wheel peak torque	N·m	90
Wheel rated torque	N·m	25

The controller smoothly switches the electronic differential torque outputs of the EMPS and DYC controllers according to the controller weight assignment results, as shown in Fig. 20(b). Figure 20(c) presents the target output torque of each electric wheel. Figure 20(d) shows that the proposed control method distributes the total target torque to each wheel, while the total traction error of electric wheels is kept small. The longitudinal motion control of the vehicle is essentially unaffected.

Figure 20(e) and 20(f) display that with the target torques output by the composite steering controller, each axle steering is tracked satisfactorily and the lateral force of each tire is always within the linear zone.

Comparing Fig. 20(h) and 20(i), it can be seen that the $\beta-\dot{\beta}$ trajectory converges in the stable region all the time under the composite steering control, while the $\beta-\dot{\beta}$ trajectory enters the unstable region under the EMPS control only. This proves the correctness of the proposed controller weight assignment module and the fact that the composite steering control is beneficial to the vehicle stability.

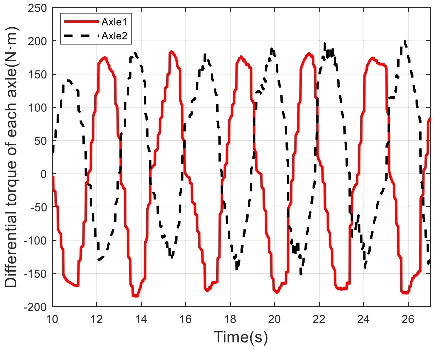

(a) Differential torque of each axle

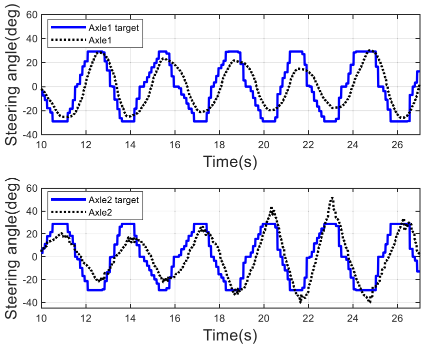

(b) Steering angle of each axle

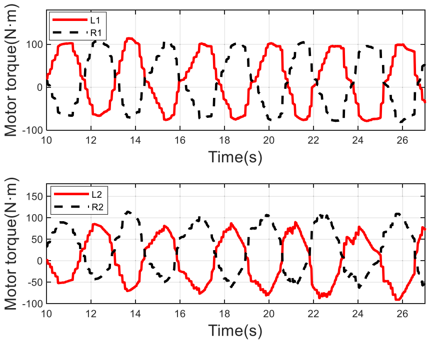

(c) Output torque of each electric wheel

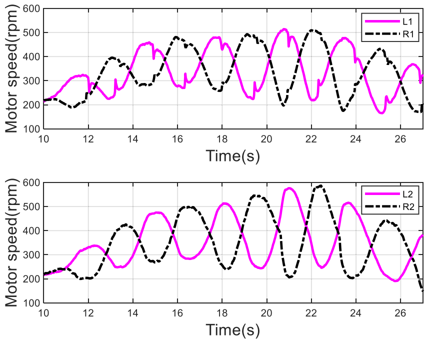

(d) Motor speed of each electric wheel

Fig. 23 EMPS steering test results

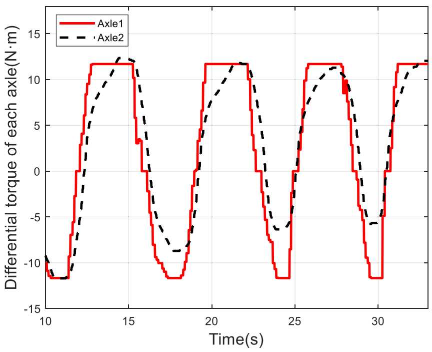

(a) Differential torque of each axle

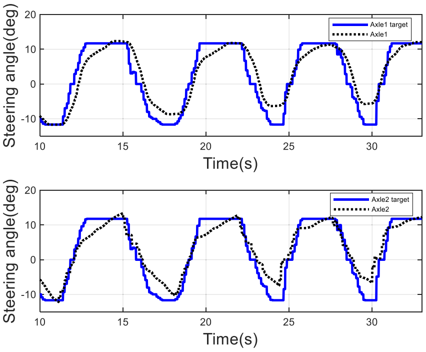

(b) Steering angle of each axle

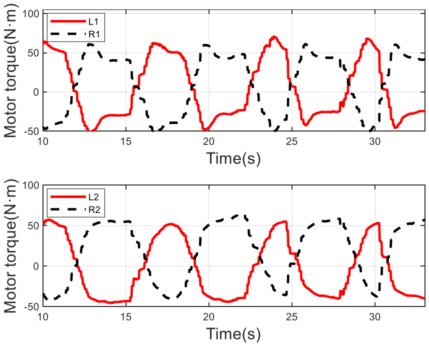

(c) Output torque of each electric wheel

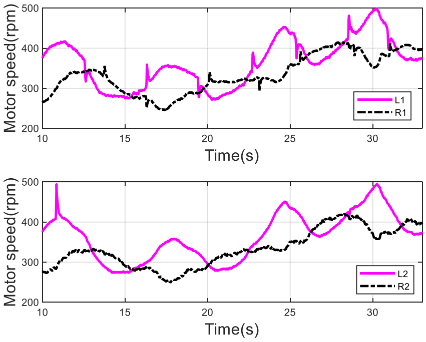

(d) Motor speed of each electric wheel

Fig. 24 EMPS omnidirectional movement test results

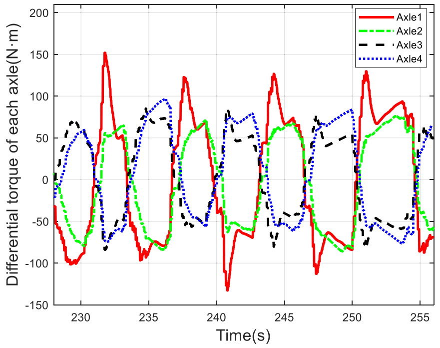

(a) Differential torque of each axle

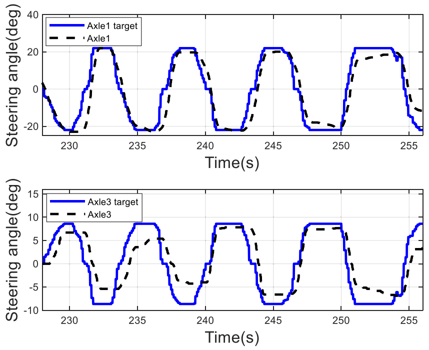

(b) Steering angle of axle 1&3

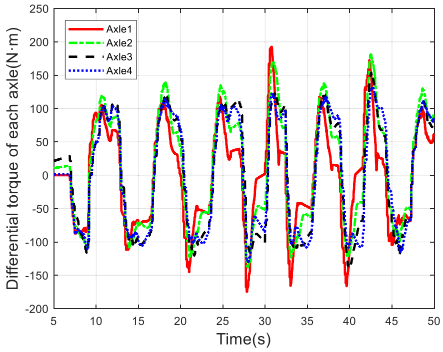

(c) Differential torque of each axle

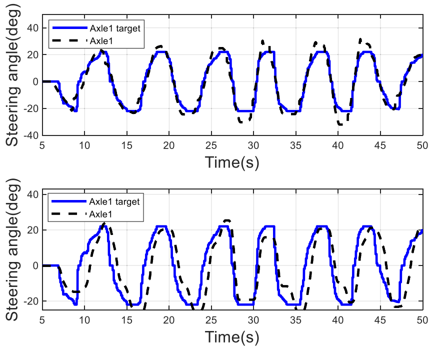

(d) Steering angle of axle 1&4

Fig. 25 EMPS test results by the four-axle test vehicle

4.2 Vehicle Test

To verify the effectiveness of the EMPS and its control strategy proposed in this paper, an 8 × 8 electric wheel independent drive all-bridge-steering test vehicle was designed. This test vehicle can be split into two units, each of which is in the form of 4 × 4 drive after splitting, and the chassis, power, and electronics are all adapted to the detachable architecture. The vehicle architecture, as depicted in Fig. 21, showcases the communication harness in red, power cables in orange, and dotted lines indicating cables or harnesses that can be connected or disconnected based on the vehicle's splitting or merging requirements. The black shaded area highlights the detachable frame structure. Visual representations of the vehicle can be observed in Fig. 22

The basic parameters of the test vehicle of 4 × 4 configuration is shown in Table 2. The test vehicle was adopted to complete the verification test of the EMPS control strategy.

Figure 23 shows a set of vehicle test curves for EMPS steering control. During the test, the mechanical steering system was disabled, and the driver manipulated the pedal position and steering wheel angle of the vehicle by remote control. Results prove that EMPS has the ability to independently implement the low-speed steering function of the vehicle.

During the vehicle test, the target steering angle calculation module for the electric drive steering axles within the upper controller is configured to ensure alignment between the target steering angles of the rear and front axles. The tracking of these target steering angles for both the front and rear axles is orchestrated through the utilization of the EMPS controller's output electronic differential torque, facilitating omnidirectional movement. Figure 24 offers a comprehensive depiction of a series of real-world vehicle test curves demonstrating the EMPS omnidirectional movement control.

The EMPS steering control test and the omnidirectional movement control test were also completed and validated on the four-axle test vehicle, yielding consistent conclusions, as illustrated in Fig. 25(a)-(b) and (c)-(d), respectively.

5 Conclusions

(1) An EKF-PF nonlinear state observer is adopted for the joint multi-objective parameter estimation of vehicles. This observer, well-suited for nonlinear systems such as vehicles, delivers enhanced estimation accuracy.

(2) By establishing and analyzing detailed vehicle and electric drive steering axle dynamics models, a multidimensional feasible domain for EMPS is proposed, ensuring the safety and smoothness of steering maneuvers.

(3) A composite steering control strategy combining EMPS and DYC is proposed. This strategy enhances steering flexibility and fault tolerance of the steering system at low speeds while maintaining vehicle stability at high speeds.
(4) The hierarchical control architecture of the proposed strategy involves the upper controller for vehicle state observation and the lower controller for steering angle tracking of EMPS, yaw rate tracking of DYC, and composite controller weight assignment.
(5) The TruckSim-Simulink co-simulation validates the effectiveness of the proposed control strategy and the accuracy of the EMPS feasible domain. Real vehicle testing confirms the efficacy of EMPS and the redundancy tolerance of the steering function in distributed drive multi-axle vehicles utilizing EMPS.

Funding This work is supported by National Key R&D Program of China (2022YFE0100100 and Nos. 52002210), Young Elite Scientists Sponsorship Program by CAST (No.2021QNRC001), and Tsinghua University postdoctoral program (Shuimu Tsinghua Scholar Program).

Declarations

Conflict of interest On behalf of all the authors, the corresponding author states that there is no conflict of interest.

References

1. Bayar, K., Unlusoy, Y.S.: Steering strategies for multi-axle vehicles. Int. J. Heavy Veh. Syst. **15**(2), 1 (2008)
2. Pan, K., Zheng, H., Wu, J., Xiao, H.: Research on steering control of multi-axle steering heavy commercial vehicle based on reducing tire wear. SAE Int. J. Veh. Dyn. Stab. NVH **4**(1), 67–80 (2020)
3. Hu, J., Li, J., Hu, Z., et al.: Energy-efficient torque-allocation strategy for a 6 × 6 vehicle using electric wheels. eTransportation **10**(1), 100136 (2021)
4. Tong, Y., Li, C., Wang, G., et al.: Integrated path-following and fault-tolerant control for four-wheel independent-driving electric vehicles. Automot. Innov. **5**(3), 311–323 (2022)
5. Guo, N., Lenzo, B., Zhang, X., et al.: A real-time nonlinear model predictive controller for yaw motion optimization of distributed drive electric vehicles. IEEE Trans. Veh. Technol. **69**(5), 4935–4946 (2021)
6. Liang, J., Lu, Y., Yin, G., et al.: A distributed integrated control architecture of AFS and DYC based on MAS for distributed drive electric vehicles. IEEE Trans. Veh. Technol. **70**(6), 5565–5577 (2021)
7. Li, S., Ma, Y., Guo, P., et al.: A study on vehicle stability control strategy with variable threshold. Automot. Eng. **37**(7), 782–787 (2015)
8. Li, H., Wang, X., Song, S., et al.: Vehicle control strategies analysis based on PID and fuzzy logic control. Proc. Eng. **137**(1), 234–243 (2016)
9. Yoshioka, T., Adachi, T., Butsuen, T.: Application of sliding-mode theory to direct yaw-moment control. JSAE Rev. **20**(4), 523–529 (1999)
10. Jing, C., Shu, H., Shu, R., et al.: Integrated control of electric vehicles based on active front steering and model predictive control. Control Eng. Pract. **121**(1), 105066 (2022)
11. Huang, G., Yuan, X., Shi, K., et al.: A BP-PID controller-based multi-model control system for lateral stability of distributed drive electric vehicle. J. Franklin Inst. **356**(13), 7290–7311 (2019)
12. Jing, H., Wang, R., Wang, J., et al.: Robust H∞ dynamic output-feedback control for four-wheel independently actuated electric ground vehicles through integrated AFS/DYC. J. Franklin Inst. **355**(18), 9321–9350 (2018)
13. Wang, J., Guo, D., Yan, T., et al.: Coordination control of differential drive assisted steering and active front steering of electric vehicle. J. Jilin Univ. (Engineering and Technology Edition) **50**(03), 776–783 (2020)
14. Wang, J., Wang, X., Luo, Z., et al.: Active disturbance rejection control of differential drive assist steering for electric vehicles. Energies **13**(10), 26–47 (2020)
15. Williams, D.E.: Generalised multi-axle vehicle handling. Veh. Syst. Dyn. **50**(1), 149–166 (2012)
16. Shuai, Z., Li, C., Gai, J., et al.: Coordinated motion and powertrain control of a series-parallel hybrid 8×8 vehicle with electric wheels. Mech. Syst. Signal Process. **120**(1), 560–583 (2019)
17. Wei, Y., Feng, X., Feng, H., et al.: State of the art for tire dynamical model research. J. Automot. Saf. Energy **5**(04), 311–323 (2014)
18. Li, H., Li, J., Hu, J., et al.: Simulation and experiment of distributed drive hybrid multi-axle heavy-duty truck dynamics control algorithm. In: Paper Presented at the 2021 China Automation Congress (CAC), Hainan, China (2022)
19. Tian, J., Zhang, C.: Research on longitudinal and lateral force coordination control of distributed drive differential steering vehicle. J. Chongqing Univ. Technol. (Natural Science) **36**(10), 21–30 (2022)
20. Scharcanski, J., Oliveira, A.B., Cavalcanti, P.G., et al.: A particle-filtering approach for vehicular tracking adaptive to occlusions. IEEE Trans. Veh. Technol. **60**(2), 381–389 (2011)
21. Li, L., Ji, H., Luo, J.: Iterated extended Kalman particle filtering. J. Xidian Univ. **02**, 233–238 (2007)
22. Chu, W., Luo, Y., Chen, L., et al.: Vehicle state estimation by unscented particle filter in distributed electric vehicle. J. Mech. Eng. **49**(24), 117–127 (2013)
23. Yang, J.: Particle Filter Algorithm Research and Application. Xi'an University of Technology, Xi'an (2008)
24. Wang, H., Jing, Z., Yang, Yan: Target tracking algorithm based on improved extend Kalman particle filter. Appl. Res. Comput. **28**(5), 1634–1636 (2011)
25. Chen, X., Guo, K.: Development for generalised multi-axle steering vehicle handling. Int. J. Heavy Veh. Syst. **27**(6), 777–799 (2020)
26. Kruse, O., Mukhamejanova, A., Mercorelli, P.: Differential steering system for vehicular yaw tracking motion with help of sliding mode control. In: Paper Presented at the 23rd International Carpathian Control Conference (ICCC), Sinaia, Romania (2022)
27. Ji, X., Wei, X., Wang, A., et al.: A novel composite adaptive terminal sliding mode controller for farm vehicles lateral path tracking control. Nonlinear Dyn. **110**(3), 2415–2428 (2022)
28. Zhang, C., Xia, Q., He, L.: A study on the influence of sideslip angle at mass center on vehicle stability. Automot. Eng. **33**(4), 277–282 (2011)